






Evidence for the Photoionization Absorption Edge in a Photospheric Radius Expansion X-Ray Burst from GRS 1747–312 in Terzan 6

Zhaosheng Li^{1,2} , Valery F. Suleimanov^{3,4,5}, Juri Poutanen^{5,6,7} , Tuomo Salmi⁶, Maurizio Falanga^{2,8} , Joonas Nättilä⁷, and Renxin Xu⁹

¹ Department of Physics, Xiangtan University, Xiangtan, 411105, People's Republic of China; lizhaosheng@xtu.edu.cn

² International Space Science Institute, Hallerstrasse 6, 3012 Bern, Switzerland

³ Institut für Astronomie und Astrophysik, Kepler Center for Astro and Particle Physics, Universität Tübingen, Sand 1, D-72076 Tübingen, Germany

⁴ Kazan (Volga region) Federal University, Kremlevskaya str. 18, Kazan 420008, Russia

⁵ Space Research Institute of the Russian Academy of Sciences, Profsoyuznaya str. 84/32, 117997 Moscow, Russia

⁶ Tuorla Observatory, Department of Physics and Astronomy, FI-20014 University of Turku, Finland

⁷ Nordita, KTH Royal Institute of Technology and Stockholm University, Roslagstullsbacken 23, SE-10691 Stockholm, Sweden

⁸ International Space Science Institute Beijing, No.1 Nanertiao, Zhongguancun, Haidian District, 100190 Beijing, People's Republic of China

⁹ School of Physics and State Key Laboratory of Nuclear Physics and Technology, Peking University, Beijing 100871, People's Republic of China

Received 2018 April 18; revised 2018 August 29; accepted 2018 August 31; published 2018 October 11

Abstract

Thermonuclear X-ray bursts on the surface of neutron stars (NSs) can enrich the photosphere with metals, which may imprint photoionization edges on the burst spectra. We report here the discovery of absorption edges in the spectra of the type I X-ray burst from the NS low-mass X-ray binary GRS 1747–312 in Terzan 6 during observations by the *Rossi X-ray Timing Explorer*. We find that the edge energy evolves from 9.45 ± 0.51 to ~ 6 keV and then back to 9.44 ± 0.40 keV during the photospheric radius expansion phase and remains at 8.06 ± 0.66 keV in the cooling tail. The photoionization absorption edges of hydrogen-like Ni, Fe, or an Fe/Ni mixture and the bound–bound transitions of metals may be responsible for the observed spectral features. The ratio of the measured absorption edge energy in the cooling tail to the laboratory value of the hydrogen-like Ni(Fe) edge energy allows us to estimate the gravitational redshift factor $1 + z = 1.34 \pm 0.11$ ($1 + z = 1.15 \pm 0.09$). The evolution of the spectral parameters during the cooling tail are well described by metal-rich atmosphere models. The combined constraints on the NS mass and radius from the direct cooling method and the tidal deformability strongly suggest very high atmospheric abundance of the iron group elements and limit the distance to the source to 11 ± 1 kpc.

Key words: binaries: general – stars: neutron – X-rays: binaries – X-rays: individual (GRS 1747-312) – X-rays: stars

1. Introduction

Neutron stars (NSs) in low-mass X-ray binaries (LMXBs) can accrete matter transferred from their companions through the Roche-lobe overflow. Depending on the mass density and temperature of the accreted gas, unstable thermonuclear burning of hydrogen, helium, or their mixture on the surface of the NSs gives rise to the phenomena known as type I X-ray bursts (e.g., see, Lewin et al. 1993; Strohmayer & Bildsten 2006 for reviews). Three main branches of type I X-ray bursts, i.e., normal bursts, intermediate-duration bursts, and superbursts, are distinguishable based on their duration (see Figure 7 in Falanga et al. 2008 and references therein). The light curves of these bursts showed a fast rise and approximately exponential decay with a duration of a few seconds for normal bursts, tens of minutes for intermediate-duration bursts, and up to several hours for superbursts, depending on the ignition depth. In particular, the superbursts are likely triggered by carbon burning in the deep NS ocean (Cumming & Bildsten 2001; in't Zand 2017).

X-ray burst spectra can usually be well fitted by a diluted blackbody, with temperature $kT_{\text{bb}} \sim 1\text{--}3$ keV (Lewin et al. 1993). Some bursts show photospheric radius expansion (PRE), which is believed to be a result of the luminosity approaching the Eddington value, when the radiation pressure lifts the NS surface layers (Lewin et al. 1993). During the subsequent cooling phase of PRE bursts, the photosphere is

likely located at the NS surface. This fact allows us to use PRE bursts as a tool to measure NS masses M and radii R (e.g., see Ebisuzaki 1987; Sztajno et al. 1987; Damen et al. 1990; van Paradijs et al. 1990; Lewin et al. 1993; Özel et al. 2009; Suleimanov et al. 2011a; Poutanen et al. 2014; Li et al. 2015, 2017). In particular, the NS LMXBs in globular clusters are ideal targets to constrain the equation of state of matter at supranuclear density, because the distance to the objects can be determined independently using optical observations (e.g., Kuulkers et al. 2003; Guillot et al. 2013; Li et al. 2015; Özel et al. 2016).

Although most X-ray burst spectra can be well described by the Planck function, deviations from the blackbody have been observed in several cases. in't Zand et al. (2013) found soft and hard X-ray excesses in the spectra of an X-ray burst from SAX J1808.4–3658, which was interpreted as a result of enhanced persistent emission during the burst. Many other LMXBs showed the same phenomenon (Worpel et al. 2013). Moreover, the reflection component from the photoionized accretion disk has been observed from the superburst in 4U 1820–30 (Ballantyne & Strohmayer 2004), 4U 1636–536, and IGR J17062–6143 (Keek et al. 2014, 2017).

Photoionization absorption features in the range 6–11 keV have also been identified in 4U 0614 + 091, 4U 1722–30, and 4U 1820–30 (in't Zand & Weinberg 2010), and *HETE* J1900.1–2455 (Kajava et al. 2017) due to the bound–bound or bound–free transitions of the newborn heavy

elements in the X-ray burst photospheres. The observed spectral features can be associated with the hydrogen-like Fe edge at 9.278 keV, or hydrogen/helium-like Ni edges at 10.8/10.3 keV. The presence of the spectral features potentially allows to measure the gravitational redshift for the NS surface (Lewin et al. 1993; Özel 2006) which gives additional constraints on the NS mass and radius.

GRS 1747–312 is a transient LMXB located in the globular cluster Terzan 6 (Predehl et al. 1991; Pavlinsky et al. 1994; Verbunt et al. 1995; in’t Zand et al. 2003a, 2003b). Thermonuclear X-ray bursts occurred in GRS 1747–312, establishing that the binary system hosts a NS. GRS 1747–312 is known to be an eclipsing binary in a 12.360 ± 0.009 hr orbit observed at an inclination of $>74.5^\circ$ with an eclipse duration of ~ 43 min (in’t Zand et al. 2000, 2003b). The optical counterpart has not yet been identified.

The distances to globular clusters can be measured from the relations (Harris 1996, 2010),

$$(m - M)_0 = V_{\text{HB}} - M_V(\text{HB}) - 3.1E(B - V), \quad (1)$$

where

$$M_V(\text{HB}) = 0.16[\text{Fe}/\text{H}] + 0.84 \quad (2)$$

and V_{HB} , $E(B - V)$ and $[\text{Fe}/\text{H}]$ are referred to as the apparent magnitude of the horizontal branch stars in a globular cluster, the foreground reddening, and the metallicity, respectively. We calculate the distance to Terzan 6 using the values and typical errors $V_{\text{HB}} = 22.16 \pm 0.20$, $E(B - V) = 2.35 \pm 0.20$, and $[\text{Fe}/\text{H}] = -0.62 \pm 0.20$ (Fahlman et al. 1995; Barbuy et al. 1997; Kuulkers et al. 2003; Valenti et al. 2007). Then, the distance uncertainty can be estimated from Equations (1) and (2) by propagating errors. The distance modulus $(m - M)_0$ is 14.13 ± 0.65 and the distance to Terzan 6 is $6.7_{-1.7}^{+2.3}$ kpc at 1 σ confidence level.

Non-Planckian spectra have also been observed in the peculiar PRE burst from GRS 1747–312 (in’t Zand et al. 2003a). The time-resolved spectra showed a strong PRE phase occurring in the first 50 s after the burst trigger. The spectra around the peak of the radius expansion and during the decay phase are biased from the blackbody profile since the reduced chi-square (χ_{red}^2) are systematically larger than 2. in’t Zand et al. (2003a) added a Gaussian line to account for the possible Fe line emission, which can improve the fitting. But the Fe line has a broad feature and a low central energy of 4.9 keV. The authors claimed that this is hard to explain from Fe–K emission within reasonable shifts, especially the larger χ_{red}^2 appears around the peak height of the photosphere where the gravitational redshift is negligible.

In this work, we investigate the possible presence of an absorption edge in this peculiar X-ray burst from GRS 1747–312 (in’t Zand et al. 2003a). The analysis of the spectral properties of the burst is given in Section 2. We discuss the origin and variations of the absorption edge energy in Section 2.2. The direct cooling method is applied to estimate the NS mass and radius in Section 3. The discussion of the results is presented in Section 4 and we summarize in Section 5.

2. Data Reduction

The Proportional Counter Array (PCA; Jahoda et al. 2006; Shaposhnikov et al. 2012) on board the *Rossini X-ray Timing*

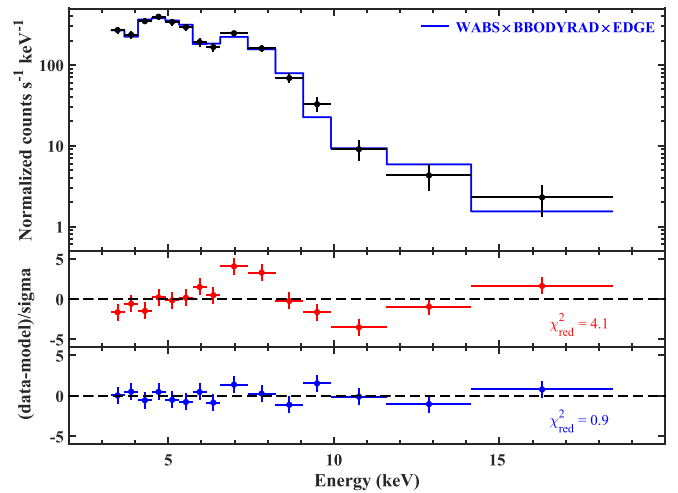


Figure 1. Spectrum of the X-ray burst observed in the time interval 28–29 s after the trigger. In the top panel, the WABS×BBODYRAD×EDGE model (blue stepped line) is displayed, while the WABS×BBODYRAD model is not shown here to avoid poor visualization. The residuals to the data are shown in the middle and bottom panels for the blackbody model and the edge model, respectively. An absorption edge improves the fit significantly.

Explorer (RXTE), which has an energy resolution of 17% at 6 keV, is a powerful instrument to study X-ray bursts. During the *RXTE* pointing to the source XTE J1751–305 (Obs. ID. 70131-02-17-00), the PCA observed an intense type I X-ray burst, which is believed to originate from GRS 1747–312 located 40′ off-axis. We re-analysed this PRE burst following in’t Zand et al. (2003a). Three proportional counter units (0, 2, 3) were active during that burst. From Standard 2 PCA data, in order to guarantee roughly the same signal-to-noise ratio for all spectra, the data were extracted with the exposure time varying from 1 to 4 s. Around 24 s after the burst trigger, the exposure time was set to 0.25 s to catch the rapid spectral variations. Following the method introduced by in’t Zand et al. (2003a), the correction to the collimator response was made due to off-axis pointing by *RXTE*. The background spectrum was extracted from 440 to 40 s before the burst trigger. Dead-time corrections were carried out according to instructions from the *RXTE* team.¹⁰ All spectra were binned to ensure each channel had at least 15 photons, and a 0.5% systematic error was added.

The spectrum of the burst shows clear deviations from the Planckian shape. An additional absorption edge improves the fits significantly (see also in’t Zand & Weinberg 2010; Kajava et al. 2017). The edge model WABS×BBODYRAD×EDGE in XSPEC (version 12.8.2) (Arnaud 1996) is applied to fit the spectra in the energy range 3–20 keV. The blackbody component, BBODYRAD, has two parameters, the blackbody temperature, kT_{bb} , and normalization, $K_{\text{bb}} \equiv (R_{\text{bb}}/D_{10\text{kpc}})^2$, to account for emission from the photosphere, where R_{bb} and $D_{10\text{kpc}}$ are the blackbody radius and the distance to the source in units of 10 kpc, respectively. The multiplicative model EDGE is expressed as $M(E) = \exp[-\tau (E/E_{\text{Edge}})^{-3}]$ for photon energies $E > E_{\text{Edge}}$ and $M(E) = 1$ otherwise, where τ and E_{Edge} are the absorption depth and the threshold energy, respectively. During the fitting, we fixed the hydrogen column density at $N_{\text{H}} = 6 \times 10^{22} \text{ cm}^{-2}$ (in’t Zand et al. 2003a). The blackbody model WABS×BBODYRAD is also used as a comparison to the edge model. We illustrate in Figure 1 how

¹⁰ https://heasarc.gsfc.nasa.gov/docs/xte/recipes/pca_deadtime.html

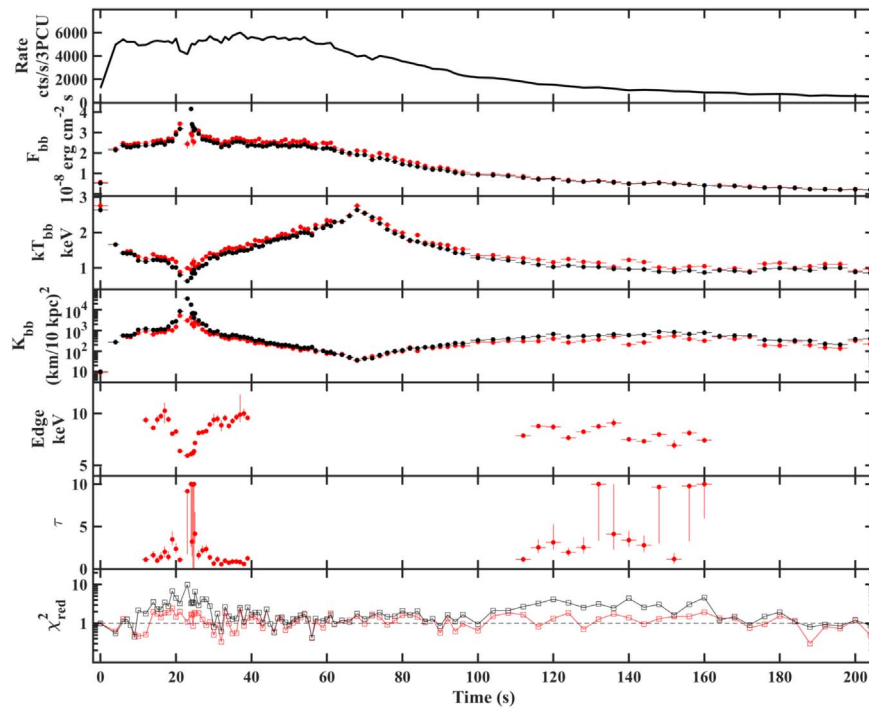


Figure 2. Time-resolved spectral parameters of the PRE burst from GRS 1747–312, which started at MJD 52394.04754. From the top to the bottom panels, the dead-time-corrected light curve of PCU 0, 2, 3, the bolometric flux, the black body temperature and normalization, the absorption edge energy, the absorption optical depth, and the reduced χ^2 are displayed. The black dots are the fitting results using the WABS×BBODYRAD model, and the red dots are from the WABS×BBODYRAD×EDGE model. All errors correspond to 1σ .

these two models fit the spectrum extracted during the PRE phase in the interval 28–29 s after the burst onset. We see a clear improvement in χ^2 and in the structure of the residuals when using the edge model. The bolometric flux is calculated using CFLUX command in the energy range 0.001–200 keV. The 1σ errors of kT_{bb} , K_{bb} , E_{Edge} , τ and flux are determined from the XSPEC command ERROR.

2.1. Results

The results of the fitting of the time-resolved spectra are shown in Figure 2, where the red crosses and black crosses are obtained from the edge model and blackbody model respectively. The χ^2_{red} are displayed in the bottom panel of Figure 2. It should be noticed that the blackbody model cannot fit the data around the peak flux ($t \sim 10$ –40 s) and the decay phase ($t \sim 110$ –160 s) very well, but we still plot the best-fitted values without errors. The blackbody model fits to the data have dozens of spectra with $\chi^2_{\text{red}} > 2$. From the edge model, only two spectra have $\chi^2_{\text{red}} > 2$ without trends in the residuals. For the multiplicative edge component, an F -stat test is appropriate to estimate the probability of chance improvement (Orlandini et al. 2012; DeCesar et al. 2013). We obtained the probability in the range 0.05 – 8×10^{-6} , which is a statistically significant improvement. Generally, the bolometric flux, the blackbody temperature, and the blackbody radius have small differences and almost the same trends compared with the blackbody model (see also Figure 3 in in’t Zand et al. 2003a).

From the spectral fitting, the touchdown flux is $F_{\text{TD}} = (2.12 \pm 0.07) \times 10^{-8} \text{ erg cm}^{-2} \text{ s}^{-1}$. Another three PRE bursts from GRS 1747–312 have lower touchdown fluxes. The two bursts observed by *RXTE* (Galloway et al. 2008) have $(1.00 \pm 0.03) \times 10^{-8}$ and $(1.67 \pm 0.04) \times 10^{-8} \text{ erg cm}^{-2} \text{ s}^{-1}$, while the burst observed by *Suzaku* (Iwai et al. 2014) has

$(1.85 \pm 0.28) \times 10^{-8} \text{ erg cm}^{-2} \text{ s}^{-1}$. Because of the strong PRE and the plateau of bolometric flux during the PRE phase, the type I X-ray burst we analyzed has been regarded as reaching its Eddington limit in previous works (e.g., in’t Zand et al. 2003a; Kuulkers et al. 2003; Galloway et al. 2008). The 3σ upper limit of the persistent luminosity for our analyzed burst is $6 \times 10^{35} \text{ erg s}^{-1}$ in the energy range 0.1–200 keV (in’t Zand et al. 2003a), which belongs to the quiescent state. In this case, the accretion disk is not expected to affect the NS atmosphere and the evolution of the spectra and the burst satisfies criteria from Suleimanov et al. (2016), i.e., the accretion luminosity less than 5% of the Eddington luminosity.

2.2. Absorption Edge

From Figure 2 we see that the edge energy evolves from 9.45 ± 0.51 to ~ 6 keV and then back to 9.44 ± 0.40 keV during the PRE phase and is 8.06 ± 0.66 keV in the cooling tail. A positive correlation between the blackbody temperature and the edge energy is clearly visible. We notice that a similar behavior of the absorption edge has been reported in 4U 0614 + 09. The metals created by thermonuclear explosion can produce the observed absorption edge (in’t Zand & Weinberg 2010). Similarly to the case of 4U 0614 + 09, the bound–bound transition might be responsible for the variations (in’t Zand & Weinberg 2010). Before and after the peak of the PRE phase, the edge energies of about 9.45 keV are consistent with the photoionization edge of the hydrogen-like Ni at 10.8 keV with redshift $z_{\text{PRE}} = 1.14 \pm 0.05$. During the cooling tail, the edge energy $E_{\text{Edge}} = 8.06 \pm 0.66$ keV corresponds to the redshift after the touchdown of $1 + z_{\text{TD}} = 1.34 \pm 0.11$ for the hydrogen-like Ni edge, if the photosphere was located at the NS surface. These estimates give us a ratio $(1 + z_{\text{TD}})/(1 + z_{\text{PRE}}) = 1.18 \pm 0.11$.

Another way to estimate this ratio from the measured fluxes in the PRE phase, F_{PRE} , and at the touchdown, F_{TD} , which satisfy the relation $F_{\text{PRE}}(1+z_{\text{PRE}}) = F_{\text{TD}}(1+z_{\text{TD}})$, if the flux in both stages, is to use the local Eddington flux. Taking the mean PRE flux $F_{\text{PRE}} = (2.69 \pm 0.26) \times 10^{-8} \text{ erg cm}^{-2} \text{ s}^{-1}$ we get $(1+z_{\text{TD}})/(1+z_{\text{PRE}}) = 1.26 \pm 0.13$, which is consistent within 1σ with the value obtained above assuming the hydrogen-like Ni/Fe origin of the edge. We therefore suggest that the absorption edges in the burst spectra come from the heavy elements, i.e., hydrogen-like Ni/Fe. Absorption edges from a mixture of Fe and Ni are also possible.

3. The Mass–Radius Constraints

We took the advantage of the direct cooling method to determine the NS mass and radius of GRS 1747–312 as proposed by Suleimanov et al. (2017). The procedure is described briefly here. We use two NS atmosphere models from Nättilä et al. (2015), with the atmosphere composition of $X = 0.352$, $Y = 0.118$, $Z = 40 Z_{\odot}$ ($Z_{\odot} = 0.0134$) for the abundances of hydrogen, helium, and metals, respectively, and the pure iron model. In these models the NS surface gravity, $\log g$, varies from 13.7 to 14.9 with a step of 0.1 for the pure iron and 0.15 for the $Z = 40 Z_{\odot}$ models. The models at intermediate $\log g$ were obtained by linear interpolation.

The direct cooling method suggests minimizing the function

$$\chi^2 = \sum_{i=1}^{N_{\text{obs}}} \left[\frac{(w\Omega - K_i)^2}{(\Delta K_i)^2} + \frac{(wf_c^4 \ell F_{\text{Edd}} - F_i)^2}{\Delta F_i^2} \right]. \quad (3)$$

Here w , f_c , and ℓ , are the model spectral dilution factor, the color correction factor, and the flux (or luminosity) in units of the Eddington limit, respectively; $\Omega = (R(1+z)/D)^2$ is the angular dilution factor and $F_{\text{Edd}} = GMc/(1+z)\kappa_{\text{T}}D^2$ is the observed Eddington flux, where $\kappa_{\text{T}} = 0.2(1+X)$ is the Thomson electron scattering opacity and X is the hydrogen mass fraction. The K_i and F_i are the i th observed blackbody normalization and flux during the cooling tail, where ΔK_i and ΔF_i are the corresponding errors. For each observed point (K_i, F_i) we take the minimum value of the normalized distance estimated in the square brackets of Equation (3) to the dense set of points along the model curve $(w\Omega, wf_c^4 \ell F_{\text{Edd}})$.

We consider a grid of masses M from 1 to $3 M_{\odot}$ with a step of $0.01 M_{\odot}$ and a grid of radii R from 9 to 18 km with a step of 0.01 km. The pairs (M, R) are ignored if the causality condition $R > 2.9GM/c^2$ is not satisfied (Lattimer & Prakash 2007). For a given pair (M, R) the surface gravity $\log g$ and the gravitational redshift z are computed. Then w and f_c are determined from the theoretical models (Nättilä et al. 2015) for the given atmosphere composition. We interpolate the sets of models to find the theoretical curve $w - wf_c^4 \ell$ for the corresponding $\log g$. Then we fit the data in the time interval $68 \leq t \leq 96$ s (see Figure 2), i.e., after the touchdown down to the flux level of $10^{-8} \text{ erg cm}^{-2} \text{ s}^{-1}$. We do not use the data at lower fluxes, because the model clearly deviates from the data (see Figure 3). We also note that the selected spectra corresponding to rather high flux and temperature are well fitted with the model without the edge (see Figure 2). This allows us to use atmosphere model spectra that have been fitted with the blackbody only to obtain w and f_c . The best-fit theoretical model computed for $\log g = 14.3$ together with the observed $K_{\text{bb}}-F_{\text{bb}}$ relation are shown in Figure 3.

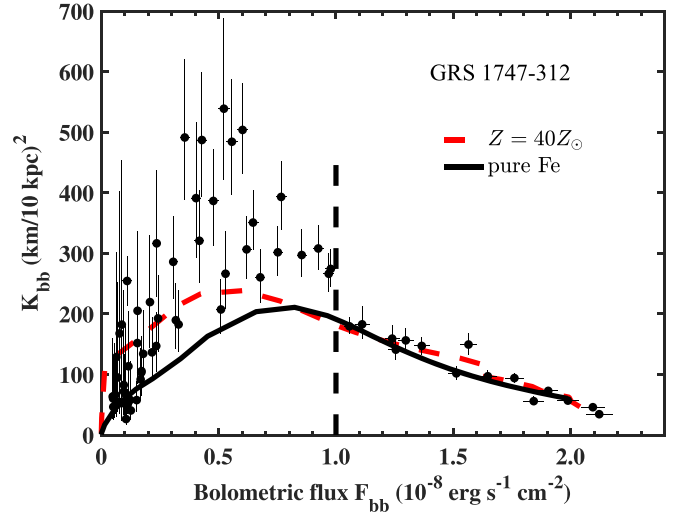


Figure 3. Blackbody normalization dependence on flux for the PRE burst. The data are shown as black dots. The solid black curve and red-dashed curve show the best-fit models for the pure iron atmosphere and $Z = 40 Z_{\odot}$ from Nättilä et al. (2015), respectively. Only the data on the right-hand side of the vertical dashed line are fitted.

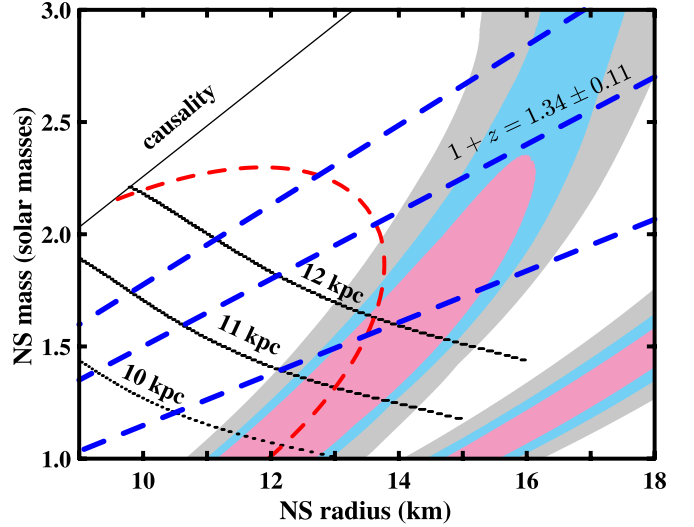


Figure 4. Mass–radius constraints for the NS in GRS 1747–312 using the pure iron (upper contours) and $Z = 40 Z_{\odot}$ (lower right contours) atmosphere models. The gray, blue, and pink contours show 68%, 90%, and 99% confidence regions, respectively. The best fit gives for 12 dof $\chi^2 = 14.66$ and 13.78, respectively, for the two models. The blue dashed lines correspond to the redshift factor $1+z = 1.34 \pm 0.11$ measured from the absorption edges. The red dashed curve shows the contour of the constant Eddington temperature $T_{\text{Edd},\infty}$ given by Equation (4) for the best-fit iron model. The black dotted curves correspond to the constant distance of 10, 11, and 12 kpc for the iron model.

We note that for a given (M, R) and chemical composition the only fitting parameter in Equation (3) is the distance to the source, D . The minimum χ^2 for each pair of (M, R) and the global minimum together with the best-fit D are obtained with the regression method. We find the best-fit $\chi^2 = 13.78$ for $Z = 40 Z_{\odot}$ and $\chi^2 = 14.66$ for pure iron (both for 12 dof). In the $M-R$ plane, $\Delta\chi^2$ can be transferred to find the confidence regions, which are shown in Figure 4. It is clear that NS radii can lie within a reasonable range of $10 < R < 14$ km (see e.g., Steiner et al. 2013; Nättilä et al. 2017) only for models with very high metal abundance, i.e., pure iron in our case. The

obtained fits also limit the possible distance to the source (see the dotted curves in Figure 4).

For illustrative purposes, we can draw a curve on the (M, R) plane corresponding to the observed Eddington temperature obtained from the best-fit parameters $F_{\text{Edd}} = 1.90 \times 10^{-8} \text{ erg cm}^{-2} \text{ s}^{-1}$ and $\Omega = 199 \text{ (km/10 kpc)}^2$ for the pure iron model shown in Figure 3. From the definition of the Eddington temperature (which is independent of the distance) we get (Suleimanov et al. 2011a):

$$T_{\text{Edd},\infty} = 9.81(F_{\text{Edd},-7}/\Omega[(\text{km}/10 \text{ kpc})^2])^{1/4} \text{ keV} \quad (4)$$

where $F_{\text{Edd},-7} = F_{\text{Edd}}/10^{-7} \text{ erg cm}^{-2} \text{ s}^{-1}$. The contour of constant Eddington temperature $T_{\text{Edd},\infty} = 1.72 \text{ keV}$ is shown in Figure 4 by the red dashed curve for the pure iron model. It is in a good agreement with the M – R confidence regions (we do not expect that they fully overlap, because the value of $T_{\text{Edd},\infty}$ is computed for $\log g = 14.3$ only and in reality varies across the (M, R) plane). Moreover, the region of constant gravitational redshift $1 + z = 1.34 \pm 0.11$ overlaps with the 68%, 90%, and 99% M – R confidence regions for the pure iron model, which means a good consistency. However, for the $Z = 40 Z_{\odot}$ model, the redshift constraints are inconsistent with the M – R confidence region (see the lower contours in Figure 4) for reasonable NS radii.

4. Discussions

In this work, we analyze the peculiar type I X-ray burst from GRS 1747–312, which showed strong discrete feature in the burst spectra. in't Zand et al. (2003a) fitted the feature by a broad emission line and claimed that two radius expansion phases, which correspondingly lasted 70 s for the slow one and 8 s for the fast one, occurred in GRS 1747–312. However, the broad emission line and the fast radius expansion phase are both difficult to explain. We found that the burst spectra are fitted well using the blackbody component with an additional photoionization edge from heavy elements. Then the presence of the fast radius expansion phase is not needed (see Figure 2).

During the cooling tail, the edge energies showed fluctuations, which cannot be solely from the limited energy resolution of *RXTE/PCA*. We note that the edge energies for the H-like Fe and H-like Ni are 9.278 keV and 10.8 keV, respectively. So we may observe gravitational redshifted edge energies between $9.278/(1+z) - 10.8/(1+z)$, i.e., 7.4–8.6 keV for $1+z = 1.26$, for a mixture of Fe/Ni. These values are close to the fluctuations, i.e., between 7.0 ± 0.4 and $9.0 \pm 0.4 \text{ keV}$. In the PRE phase, the edge energies are systematically larger than those during the cooling tail, which may indicate changes in edge energy from the gravitational redshift variations.

4.1. Reason for the Vanishing of the Photoionization Edge around the Touchdown

Close to the touchdown, i.e., $t \sim 40$ – 110 s after the burst onset, the blackbody model can fit the spectra very well, which means the photoionization edge component is unnecessary. A similar vanishing of the photoionization edge was also observed in 4U 0614 + 091, 4U 1722–30, 4U1820–30 and *HETE* J1900.1–2455 (in't Zand & Weinberg 2010; Kajava et al. 2017). The absence of edges is easy to understand because at high temperatures the metals (Fe or Ni) in the NS atmosphere are fully ionized. On another hand, the

photoionization edge appeared again $t \sim 110$ – 160 s after the burst onset. At this time, the temperature was much lower ($\sim 1 \text{ keV}$, see Figure 2) and the iron in the NS atmosphere was only partially ionized.

4.2. Possibility of an Expansion Phase in the Cooling Tail

At fluxes smaller than $10^{-8} \text{ erg cm}^{-2} \text{ s}^{-1}$, the blackbody normalization, K_{bb} , is about two times larger than the model predicts. If we interpret this as evidence for an extended atmosphere, this would have two consequences. First, the radius of an atmosphere larger than R_{NS} would produce a larger K_{bb} . If we accept the radius of the NS to be 13 km (as measured for $M_{\text{NS}} = 1.5 M_{\odot}$ from the spectral evolution at higher fluxes) and $1+z = 1.23$, the atmosphere radius at low fluxes is about 18 km, corresponding to $1+z = 1.15$, if the color correction factor variation is ignored. Second, the theoretical relation $K_{\text{bb}}-F_{\text{bb}}$ is derived from the plane-parallel assumption, which is not satisfied for an extended atmosphere (Suleimanov et al. 2011b; Nättilä et al. 2015). A second photospheric expansion phase may arise due to an increase of the radiation pressure when the heavy elements are not fully ionized, as we observe at the absorption edge. Because in our atmosphere model we do not take into account spectral lines and photoionization from the excited levels, the additional sources of opacity can, potentially, lead to atmospheric expansion. In this case, the true gravitational redshift should be larger than the measured value.

4.3. Effect of Ignorance of NS Spin

In this work, the effects of NS spin were ignored. Actually, the rotation of the NS can smear the absorption edge, which can be fitted by the SMEDGE model in XSPEC (di Salvo et al. 2009) or by the DPSMEDGE model (Iwai et al. 2017). The SMEDGE model, with the photoionization cross-section index fixed at -3 , was also applied to account for the absorption. We found that E_{edge} is well consistent with the pure edge model, while the optical depth, τ , is slightly larger. Statistically, the SMEDGE cannot provide better reduced χ^2 than the EDGE model. Moreover, the estimation of gravitational redshift only depends on the measured energy, so ignorance of it would not affect our conclusions.

4.4. M–R of the NS in GRS 1747–312

The spectral data for the X-ray burst cooling tail from GRS 1747–312 are not of sufficient quality to place tight constraints on the NS mass and radius. Therefore, additional independent information on the NS properties should be used. The detection of a gravitational wave from an NS–NS merger sheds new light on the NS equation of state (Abbott et al. 2017). The 90% confidence limit on the tidal deformability $\Lambda < 800$ of a $1.4 M_{\odot}$ NS implies an NS radius below $\sim 13.6 \text{ km}$ for $M_{\text{NS}} > 0.5 M_{\odot}$ (Annala et al. 2018). For the $Z = 40 Z_{\odot}$ model, the obtained lower limit on the NS radius of 14 km strongly contradicts this condition. A higher metal abundance with $>40 Z_{\odot}$ may be produced in the atmosphere during the long PRE phase of the studied burst. For example, the NS mass–radius constraints obtained with pure iron models, combined with the condition $R < 13.6 \text{ km}$, imply a 90% confidence upper limit on the NS mass in GRS 1747–312 of $1.8 M_{\odot}$.

4.5. Distance to GRS 1747–312/Terzan 6

Optical measurements of the distance to Terzan 6 have been reported by several teams. With the calculated foreground reddening to Terzan 6 $E(B - V) = 2.04$, and the metallicity $[\text{Fe}/\text{H}] = -0.6$ adopted from the similar globular cluster M71, the distance to Terzan 6 was measured to be 6.8 ± 0.46 kpc (see Fahlman et al. 1995 and references therein). Barbuy et al. (1997) obtained $E(B - V) = 2.24$ and $V_{\text{HB}} \approx 22.25$, which leads to a distance of 7 kpc to Terzan 6. Valenti et al. (2007) found $E(B - V) = 2.35$ and a distance of 6.7 kpc from the color-magnitude diagram observed by the ESO Max-Planck-Institut 2.2 m telescope. Kuulkers et al. (2003) quoted a distance $9.5_{-2.5}^{+3.3}$ kpc to Terzan 6 from the globular cluster catalog by Harris (1996), in which $E(B - V) = 2.14$ was adopted. This distance estimate is larger than other measurements and the distance of 6.8 kpc given in the updated catalog by Harris (2010).¹¹ From Equations (1) and (2), the foreground reddening, $E(B - V)$, contributed the largest discrepancy.

The distance to GRS 1747–312 can also be constrained by the direct cooling tail method and for the pure iron model we get $D = 11 \pm 1$ kpc (see the dotted curves in Figure 4), taking into account additional constraints on the radius. This distance is larger than that measured from optical observations, i.e., $6.7_{-1.7}^{+2.3}$ kpc. There exist a number of possible reasons for this discrepancy. If the NS surface is partially blocked by the accretion disk, i.e., one third of the NS surface is visible, the inferred distance from the direct cooling method should be 6.7 kpc instead of 11.5, while the $M-R$ contours are unchanged. But it is difficult to imagine that the disk may have such a sharp boundary in the quiescent state. The errors of V_{HB} , $E(B - V)$ and $[\text{Fe}/\text{H}]$ are assigned rather than observed, and therefore may be underestimated. Moreover, the uncertainties in the coefficients of the empirical relations (1) and (2) are not taken into account, which will lead to a larger uncertainty in the distance. Otherwise, an NS with mass smaller than $1 M_{\odot}$ is needed.

5. Conclusion



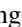
The PRE burst we studied is the most intense of all bursts from GRS 1747–312 (in't Zand et al. 2003b; Galloway et al. 2008; Iwai et al. 2014). We find that the edge observed during the PRE phase and the cooling tail correspond to absorption from hydrogen-like Fe, Ni, or a mixture of Fe and Ni. The presence of the edge is confirmed by fits to the observed flux-normalization relation with the theoretical model, which requires a high metal abundance.

We showed that the $M-R$ confidence region for even such a high metal abundance as $40 Z_{\odot}$ is inconsistent with the recent constraints on the NS radius of <13.6 km coming from tidal deformability during an NS–NS merger. However, the $M-R$ constraints obtained for pure iron are well consistent with this limit, giving an upper limit on the mass of the NS of $1.8 M_{\odot}$. These constraints are also consistent with the gravitational redshift measurements from the absorption edge. The data then limit the distance to the source to $D = 11 \pm 1$ kpc. Future measurements of the mass function and type of the companion star would help to improve the constraints on the NS mass and radius in GRS 1747–312.

We appreciate the referee for the comments and suggestions for improving our work. Z.L. thanks Tadayasu Dotani for the useful discussions. Z.L. was supported by the Swiss Government Excellence Scholarships. Z.L. thanks the International Space Science Institute and University of Bern for the hospitality. Parts of this work have been done during Z.L.'s visits to the University of Turku and the University of Tübingen. This work was supported by the National Key R&D Program of China (No. 2017YFA0402602), the National Natural Science Foundation of China (Grant Nos. 11703021, 1673002 and U1531243), and Hunan Provincial Natural Science Foundation of China (Grant Nos. 2017JJ3310 and 2018JJ3495). This research has been supported in part by the grant 14.W03.31.0021 of the Ministry of Education and Science of the Russian Federation (J.P., V.F.S.) and by the Deutsche Forschungsgemeinschaft grant WE 1312/51-1 (V.F.S.).

Software: Xspec (v12.8.2; Arnaud 1996).

ORCID iDs

Zhaosheng Li  <https://orcid.org/0000-0003-2310-8105>
 Juri Poutanen  <https://orcid.org/0000-0002-0983-0049>
 Maurizio Falanga  <https://orcid.org/0000-0003-3095-6065>

References

- Abbott, B. P., Abbott, R., Abbott, T. D., et al. 2017, *PhRvL*, **119**, 161101
 Annala, E., Gorda, T., Kurkela, A., & Vuorinen, A. 2018, *PhRvL*, **120**, 172703
 Arnaud, K. A. 1996, in ASP Conf. Ser. 101, *Astronomical Data Analysis Software and Systems V*, ed. G. H. Jacoby & J. Barnes (San Francisco, CA: ASP), 17
 Ballantyne, D. R., & Strohmayer, T. E. 2004, *ApJL*, **602**, L105
 Barbuy, B., Ortolani, S., & Bica, E. 1997, *A&AS*, **122**, 483
 Cumming, A., & Bildsten, L. 2001, *ApJL*, **559**, L127
 Damen, E., Magnier, E., Lewin, W. H. G., et al. 1990, *A&A*, **237**, 103
 DeCesar, M. E., Boyd, P. T., Pottschmidt, K., et al. 2013, *ApJ*, **762**, 61
 di Salvo, T., D'Aí, A., Iaria, R., et al. 2009, *MNRAS*, **398**, 2022
 Ebisuzaki, T. 1987, *PASJ*, **39**, 287
 Fahlman, G. G., Douglas, K. A., & Thompson, I. B. 1995, *AJ*, **110**, 2189
 Falanga, M., Chenevez, J., Cumming, A., et al. 2008, *A&A*, **484**, 43
 Galloway, D. K., Muno, M. P., Hartman, J. M., Psaltis, D., & Chakraborty, D. 2008, *ApJS*, **179**, 360
 Guillot, S., Servillat, M., Webb, N. A., & Rutledge, R. E. 2013, *ApJ*, **772**, 7
 Harris, W. E. 1996, *AJ*, **112**, 1487
 Harris, W. E. 2010, arXiv:1012.3224
 in't Zand, J. 2017, in RIKEN Symp., 7 Years of MAXI: Monitoring X-Ray Transients, <http://adsabs.harvard.edu/abs/2017symp.conf..121I>
 in't Zand, J. J. M., Strohmayer, T. E., Markwardt, C. B., & Swank, J. 2003a, *A&A*, **409**, 659
 in't Zand, J. J. M., & Weinberg, N. N. 2010, *A&A*, **520**, A81
 in't Zand, J. J. M., Bazzano, A., Cocchi, M., et al. 2000, *A&A*, **355**, 145
 in't Zand, J. J. M., Hulleman, F., Markwardt, C. B., et al. 2003b, *A&A*, **406**, 233
 in't Zand, J. J. M., Galloway, D. K., Marshall, H. L., et al. 2013, *A&A*, **553**, A83
 Iwai, M., Dotani, T., Ozaki, M., et al. 2014, in *Suzaku-MAXI 2014: Expanding the Frontiers of the X-ray Universe*, ed. M. Ishida, R. Petre, & K. Mitsuda, 158
 Iwai, M., Dotani, T., Ozaki, M., et al. 2017, *PASJ*, **69**, 61
 Jahoda, K., Markwardt, C. B., Radeva, Y., et al. 2006, *ApJS*, **163**, 401
 Kajava, J. J. E., Nättälä, J., Poutanen, J., et al. 2017, *MNRAS*, **464**, L6
 Keek, L., Ballantyne, D. R., Kuulkers, E., & Strohmayer, T. E. 2014, *ApJL*, **797**, L23
 Keek, L., Iwakiri, W., Serino, M., et al. 2017, *ApJ*, **836**, 111
 Kuulkers, E., den Hartog, P. R., in't Zand, J. J. M., et al. 2003, *A&A*, **399**, 663
 Lattimer, J. M., & Prakash, M. 2007, *PhR*, **442**, 109
 Lewin, W. H. G., van Paradijs, J., & Taam, R. E. 1993, *SSRv*, **62**, 223
 Li, Z., Falanga, M., Chen, L., Qu, J., & Xu, R. 2017, *ApJ*, **845**, 8
 Li, Z.-S., Qu, Z.-J., Chen, L., et al. 2015, *ApJ*, **798**, 56
 Nättälä, J., Miller, M. C., Steiner, A. W., et al. 2017, *A&A*, **608**, A31

¹¹ <http://physwww.mcmaster.ca/~harris/mwgc.dat>

- Nättilä, J., Suleimanov, V. F., Kajava, J. J. E., & Poutanen, J. 2015, *A&A*, **581**, A83
- Orlandini, M., Frontera, F., Masetti, N., Sguera, V., & Sidoli, L. 2012, *ApJ*, **748**, 86
- Özel, F. 2006, *Natur*, **441**, 1115
- Özel, F., Güver, T., & Psaltis, D. 2009, *ApJ*, **693**, 1775
- Özel, F., Psaltis, D., Güver, T., et al. 2016, *ApJ*, **820**, 28
- Pavlinsky, M. N., Grebenev, S. A., & Sunyaev, R. A. 1994, *ApJ*, **425**, 110
- Poutanen, J., Nättilä, J., Kajava, J. J. E., et al. 2014, *MNRAS*, **442**, 3777
- Predehl, P., Hasinger, G., & Verbunt, F. 1991, *A&A*, **246**, L21
- Shaposhnikov, N., Jahoda, K., Markwardt, C., Swank, J., & Strohmayer, T. 2012, *ApJ*, **757**, 159
- Steiner, A. W., Lattimer, J. M., & Brown, E. F. 2013, *ApJL*, **765**, L5
- Strohmayer, T., & Bildsten, L. 2006, in *Compact stellar X-ray sources*, ed. W. Lewin & M. van der Klis (Cambridge: Cambridge Univ. Press), 113
- Suleimanov, V., Poutanen, J., Revnivtsev, M., & Werner, K. 2011a, *ApJ*, **742**, 122
- Suleimanov, V., Poutanen, J., & Werner, K. 2011b, *A&A*, **527**, A139
- Suleimanov, V. F., Poutanen, J., Klochkov, D., & Werner, K. 2016, *EPJA*, **52**, 20
- Suleimanov, V. F., Poutanen, J., Nättilä, J., et al. 2017, *MNRAS*, **466**, 906
- Sztajno, M., Fujimoto, M. Y., van Paradijs, J., et al. 1987, *MNRAS*, **226**, 39
- Valenti, E., Ferraro, F. R., & Origlia, L. 2007, *AJ*, **133**, 1287
- van Paradijs, J., Dotani, T., Tanaka, Y., & Tsuru, T. 1990, *PASJ*, **42**, 633
- Verbunt, F., Bunk, W., Hasinger, G., & Johnston, H. M. 1995, *A&A*, **300**, 732
- Worpel, H., Galloway, D. K., & Price, D. J. 2013, *ApJ*, **772**, 94